JGR Oceans

RESEARCH ARTICLE
10.1029/2019JC015577

Special Section:
The Three Major Hurricanes of 2017: Harvey, Irma and Maria

# Coastal Inundation Mapping From Bitemporal and Dual-Polarization SAR Imagery Based on Deep Convolutional Neural Networks

**Bin Liu[1], Xiaofeng Li[2], and Gang Zheng[3]**

[1]College of Marine Sciences, Shanghai Ocean University, Shanghai, China, [2]GST at NOAA/NESDIS, College Park, MD, USA, [3]The State Key Laboratory of Satellite Ocean Environment Dynamics, Second Institute of Oceanography, Ministry of Natural Resources, Hangzhou, China

**Key Points:**
- A deep learning-based method is proposed for accurate coastal inundation mapping in radar imagery
- Geospatial and temporal analyses of coastal inundation caused by 2017 Hurricane Harvey are performed
- The wind-influence analysis and cost-sensitive losses contribute to more practical mapping models

**Correspondence to:**
X. Li,
xiaofeng.li@ieee.org

**Citation:**
Liu, B., Li, X., & Zheng, G. (2019). Coastal Inundation Mapping From Bitemporal and Dual-Polarization SAR Imagery Based on Deep Convolutional Neural Networks. *Journal of Geophysical Research: Oceans*, *124*, 9101–9113. https://doi.org/10.1029/2019JC015577

Received 20 AUG 2019
Accepted 2 OCT 2019
Accepted article online 07 NOV 2019
Published online 17 DEC 2019



**Abstract** This study develops an effective and robust method to mine bitemporal and dual-polarization synthetic aperture radar (SAR) imagery information for coastal inundation mapping, based on deep convolutional neural networks. The specially tailored deep convolutional neural network-based SAR coastal flooding mapping network (SARCFMNet) leverages two modifications to improve the accuracy and robustness: the physics-aware input information design and the regularization. The proposed SARCFMNet is applied to the mapping and impact analysis of the coastal inundation caused by 2017 Hurricane Harvey near Houston, Texas, USA. Six pairs of Sentinel-1 SAR images are analyzed along with corresponding ground truth data from Copernicus Emergency Management Service Rapid Mapping products and land-cover types from Google Earth and OpenStreetMap. Flooded areas of 4,000 $km^2$ are extracted and analyzed. In an analyzed scene, 76% of the flooded area was agriculture area like pasture and cultivated crops field. A flooding map series shows the inundation shrinking rate is about 1% of the analyzed scene per day after the passage of Harvey. However, there was a delayed inundation in Glen Flora, Texas, after the heavy raining period. The average mapping accuracy and F1 score, that is, the harmonic mean of recall and precision, are 0.98 and 0.88, respectively. The impact of wind and cost-sensitive loss functions on the development of SARCFMNet is also discussed. This study demonstrates the proposed method can accurately map hurricane-induced inundation. The method can also be readily extended to other multitemporal SAR imagery classification applications.

**Plain Language Summary** Coastal flooding caused by hurricanes has a huge impact on the safety and properties of people in coastal areas. Coastal flooding mapping using synthetic aperture radar (SAR) data is a low-cost and wide-coverage means; moreover, SAR has day-and-night, all-weather observation abilities. High-accuracy and robust coastal flooding mapping from SAR imagery information will help the management to formulate more targeted responses and the researchers to better understand coastal flooding mechanisms and develop more precise forecasting models. Based on deep convolutional neural networks, a specially tailored SAR coastal flooding mapping network method is developed to mine bitemporal and dual-polarization SAR imagery information for coastal flooding mapping. The performance of the proposed SAR coastal flooding mapping network is demonstrated by mapping the coastal flooding near Houston, Texas, USA, after 2017 Hurricane Harvey. The study verifies that the mapping accuracy and robustness of the proposed method are better than those of the classic and widely applied deep convolutional neural network method and also shows the mapping products contribute to a better understanding of the geospatial and temporal characteristics of coastal flooding.

## 1. Introduction

Coastal flooding caused by hurricanes is an example of compound hazards. It is the combination of storm surge and rainfall-induced freshwater river flooding. Coastal flooding has a huge impact on safety and properties of people in coastal areas. For example, 2017 Hurricane Harvey stalled over the heavily populated Houston area on 26–28 August and brought extreme precipitation. This resulted in unprecedented flooding with over 80 fatalities (van Oldenborgh et al., 2017). According to the National Hurricane Center, Harvey caused over 125 billion dollars of damage, making it the second-costliest hurricane ever recorded in the United States.

Unfortunately, coastal flooding could get even worse in the future. Higher temperature may contribute to higher moisture in the atmosphere and increasing the flood's severity (Vahedifard et al., 2016). Patricola and Wehner (2018), using simulations, found that climate change had enhanced the average and extreme rainfall of hurricanes Katrina, Irma, and Maria. Human activities, such as land-cover changes and urbanization, can intensify the impact of coastal flooding on infrastructure (Bilskie et al., 2014). W. Zhang et al. (2018) found that urbanization exacerbated not only the flood response but also the hurricane total rainfall. These studies should make us alert for the intensified flooding on the highly urbanized and heavily populated coastal areas.

In this context, high-accuracy mapping of hurricane-induced coastal inundation is needed to assist coastal managers to make better planning and researchers to better understand coastal inundation mechanisms and develop more precise forecasting models (Hostache et al., 2018). Common methods for this task include ground surveying and remote sensing (RS)-based information extraction. Ground surveying is direct and accurate, but it is very costly and there are some inaccessible areas. Coastal inundation mapping from RS data is a low-cost way, and it can cover all the potential flooded areas. According to different platforms, RS-based mapping can be mainly divided into aerial and satellite RS-based means. The aerial RS-based means may be limited by weather reasons. According to different sensors, RS-based mapping can be mainly divided into optical- and synthetic aperture radar (SAR)-based means. Compared to optical images, SAR images are difficult to understand. However, SAR is sensitive to surface water and can provide an all-weather, day-and-night observation means. Therefore, in this study, we focus on the coastal inundation mapping from satellite-based SAR imagery. The Sentinel-1 SAR satellites provide a free and open data source for this study.

The coastal inundation mapping from SAR images can be divided into three main types of methods. The first type is traditional segmentation and classification of SAR backscattering information, including histogram thresholding (Chini et al., 2017), active contour (Horritt, 1999), region growing (Matgen et al., 2011), change detection (Bazi et al., 2005), and statistical modeling (Giustarini et al., 2016). The second type is based on the target decomposition theorem of polarimetric SAR images (Park et al., 2013; Plank et al., 2017; Sato et al., 2012). These two types of methods use human-crafted and predefined features for pattern classification in SAR backscattering or polarimetric information. Their problems of achieving robust flooding mapping are rooted in different influential factors: (1) speckle noise of SAR images; (2) SAR system factors from the incidence angle and polarization; (3) meteorological influences from wind and rainfall; and (4) environmental influences from buildings, dense vegetation, and water-like areas. The third type, the deep convolutional neural network (DCNN)-based methods, is promising for solving these problems. For the DCNN models, an advanced type of deep learning models, the features useful for robust classification are dug out from data, instead of being predefined. This idea is repeatedly verified in the computer vision community (Russakovsky et al., 2015) as well as in the geophysics community (Reichstein et al., 2019; J. Zhang et al., 2018; Anantrasirichai et al., 2018). There are several existing studies for DCNN-based flooding mapping. Multi$^3$Net was proposed for flooded buildings extraction (Rudner et al., 2018). This study inherited the idea from building footprint extraction in urban areas. It is essential to merge postevent very high resolution optical images into the framework, but this data source is difficult to obtain in disasters like hurricanes. Kang et al. (2018) verified that the DCNN-based flooding detection method is more accurate than the aforementioned Type-1 and -2 methods for SAR images, but this study treated each temporal and each polarization SAR image separately.

Considering that the DCNN models have the potential to solve the problems of robust inundation mapping, we develop a DCNN-based SAR coastal flooding mapping network (SARCFMNet). The SARCFMNet is a specially tailored model for SAR coastal inundation mapping. It contains two modifications to improve accuracy and robustness: (1) the physics-aware input information design integrates SAR RS physics of flooding mapping with the DCNN framework and fuses temporal and polarimetric information for more robust mapping and (2) the regularization design improves the model's generalization ability. The proposed SARCFMNet is applied to the mapping and impact analysis of the coastal inundation caused by 2017 Hurricane Harvey near Houston, Texas, USA. Six pairs of Sentinel-1 SAR images are analyzed along with corresponding ground truth data from Copernicus Emergency Management Service (EMS) Rapid Mapping products (Copernicus EMS Rapid Mapping, n.d.) and land-cover types from Google Earth and OpenStreetMap. In these images, the flooded areas with a size of about 4,000 km$^2$ are extracted and analyzed.

The contributions of this study include

- The SARCFMNet shows better and more robust performance, compared to the classic and widely applied DCNN method. This confirms the physics-aware input information and regularization designs can improve the accuracy and robustness of the DCNN models for inundation mapping, and other applications involving multitemporal SAR image classification.
- Based on the mapping products, the geospatial and temporal characteristics of the coastal flooding caused by Harvey is analyzed and discussed.
- The wind influence is discovered in the DCNN-based method, which indicates the DCNN models taking into account wind influence will be more robust in practical use.
- The cost-sensitive losses for the DCNN-based coastal flooding mapping are explored, which is useful for more adaptive models considering performance costs.

## 2. Data

Hurricane Harvey affected Houston area from the end of August to the beginning of September 2017. During this period, we acquire six pairs of Sentinel-1 SAR images with VV + VH dual-polarization in the study region, five pairs with the Interferometric Wide (IW) swath mode, and one pair with the Stripmap (SM) mode. The Sentinel-1 data are free and publically available. The parameters of the data used in this study are listed in Table 1. The actual coverage areas of the SAR images are larger than the coverage areas listed in the table. This is because we cut the images to geographically match the preevent and postevent images. It is worth noting that the postevent image of the IW01 pair is influenced by wind. Harvey that degenerated to tropical storm still brought strong wind to the scene covered by the postevent image of the IW01, about 20 m/s (Weather Underground, n.d.). The ground truth is delineated with the help of Copernicus Emergency Management Service Rapid Mapping products (Copernicus EMS Rapid Mapping, n.d.) and land-cover types from Google Earth and OpenStreetMap.

Figure 1 gives a visual illustration for the SM01 pair as an example. Subfigures (a) and (b) are the preevent and postevent images for the VV polarization, respectively. Subfigures (d) and (e) are the preevent and postevent images for the VH polarization, respectively. Subfigures (c) and (f) are the pseudo color images for the VV and VH polarizations, respectively. In the red-green-blue pseudo color image, the blue channel represents the normalized radar cross section (NRCS) information of the preevent image, the red channel represents the NRCS information of the postevent image, and the green channel represents the difference information between the postevent and preevent NRCS. The NRCS and difference information will be described in the next section. In the pseudo color images, the flooding areas are highlighted in blue. Subfigures (g) and (h) are the Google Earth image and OpenStreetMap of the area covered by the SM01 pair, respectively. We can see that the SM01 covers Houston and its western and southern neighboring areas.

## 3. Methodology

### 3.1. Preprocessing

The aim of the preprocessing is to prepare data for training and testing. It is composed of the following steps:

1. Apply orbit file: It provides the accurate satellite orbit file for the SAR product.
2. Sliding-window filtering: A $7 \times 7$ sliding-window filter was applied to all SAR images.
3. Radiometric calibration: It is applied to the SAR image so that the pixel values after calibration truly represent the radar backscattering information of the reflecting surface. It converts the SAR image information to the NRCS information ($\sigma^0$).
4. To dB: The $\sigma^0$ is converted to decibel ($\sigma^0_{\mathrm{dB}}$, logarithmic scale).
5. Range-Doppler terrain correction: It geocodes the SAR image ($\sigma^0_{\mathrm{dB}}$) into a geographic coordinate system (World Geodetic System 84) and masks out ocean areas with the digital elevation model information. After the conversion, pixel spacing in this study is $8.9832 \times 10^{-5\circ}$ in both latitude and longitude.
6. Subset generation: For each pair listed in Table 1, since the preevent and postevent SAR images are both converted into the same geographic coordinate system. We cut the subsets using the same coverage area (listed in Table 1) from the preevent and postevent images. The subsets are matched geographically.

**Table 1**
*Sentinel-1 Data Used in This Study*[a]

| | Preevent time[b] | Postevent time[b] | Coverage[c] | Pixel spacing | Sample number |
|---|---|---|---|---|---|
| IW01 | 08–05, 00:26 | 08–29, 00:26[d] | N29.5°W96.75°, N28.75°W95.0° | 10 m | 1973 |
| IW02 | 08–05, 00:26 | 08–29, 00:26 | N31.0°W97.25°, N30.0°W95.0° | 10 m | 1384 |
| IW03 | 07–31, 00:18 | 09–05, 00:18 | N30.5°W95.25°, N29.5°W92.75° | 10 m | 1769 |
| IW04 | 08–24, 12:22 | 09–05, 12:22 | N30.5°W97.0°, N29.0°W94.75° | 10 m | 1746 |
| IW05 | 08–18, 12:22 | 08–30, 12:22 | N30.5°W97.0°, N29.25°W94.75° | 10 m | 2184 |
| SM01 | 08–23, 12:30 | 09–04, 12:30 | N30.25°W96.25°, N29.0°W95.25° | 10 m | 993 |

[a]They are all from Sentinel-1 Ground Range Detected products. [b]The time form is MM-DD, hh:mm Coordinated Universal Time (UTC). [c]The coverage is represented by up-left and down-right geographical coordinates. [d]The postevent image is influenced by wind.

It is worth mentioning that the above preprocessing procedure is implemented by the Sentinel Application Platform software. It can be easily reproduced and revised. After the preprocessing, the preevent and postevent image coverages are geometrically matched. Each pair is cut into 256 × 256, nonoverlapping samples. If the ratio of the flooding area to the sample size is lower than $1 \times 10^{-4}$, this sample is not considered for sparsity. The sample number of each pair is listed in Table 1.

### 3.2. SARCFMNet Design

The SARCFMNet method is based on the U-Net framework (Ronneberger et al., 2015) for U-Net's verified effectiveness in the research community. The SARCFMNet is shown in Figure 2. The U-shaped network consists of two paths: an encoding path to reduce the spatial size and extract high-level feature information for accurate classification, and a decoding path to combine the feature and spatial information with a sequence of upsampling and concatenations with high-resolution features. As shown in Figure 2, the encoding path (left part) is composed of 3 × 3 convolutions with the rectified linear unit (ReLU) activation and 2 × 2 pooling processes. The decoding path (right part) is composed of 2 × 2 upsampling processes and 3 × 3 convolutions with the ReLU activation. The concatenations fuse multiscale feature information. The numbers near the pooling and upsampling processes indicate the dimensions of the features before the processes. The coastal flooding mapping problem is essentially a binary, pixel-wise classification problem. Therefore, as shown in Figure 2, the last layer of the network is a 1 × 1 convolution with the Sigmoid activation. The loss function is the binary cross entropy (BCE) for binary classification (Lin et al., 2017). The performance evaluation metric is pixel-wise classification accuracy.

It is worth noting that, in the SARCFMNet, we made two specially tailored modifications to U-Net (Figure 2). The first modification is the physics-aware input information design. For this study, we consider six different input information designs listed in Figure 2. In this figure, $\sigma$ represents the NRCS. Its superscript indicates preevent or postevent. Its subscript indicates VV or VH polarization. Directly, bitemporal SAR information with single polarization, denoted as VV or VH, is often used in the related studies (Chini et al., 2017; Giustarini et al., 2016; Kang et al., 2018). In this study, for the input information design, based on the radar RS physics, we have two considerations: (1) the VV and VH polarization information should be fused, for they can compensate each other; and (2) $\sigma^{post}_{VV} - \sigma^{pre}_{VV}$ and $\sigma^{post}_{VH} - \sigma^{pre}_{VH}$; that is, the difference images for the VV and VH polarizations, respectively, should be added. From the preprocessing, we know $\sigma^{post}_{VV} - \sigma^{pre}_{VV}$ and $\sigma^{post}_{VH} - \sigma^{pre}_{VH}$ represent the log ratios of intensity for the VV and VH polarizations, respectively. The log ratio is an important information source for SAR image change detection (Bazi et al., 2005). Based on the above two considerations, for the SARCFMNet, we propose to use the input information design denoted as DUAL+Diff listed in Figure 2. The DUAL+Diff design fuses bitemporal, log ratio, and dual-polarization information sources together and includes them in the DCNN framework. Inclusion of these information sources integrates the SAR RS physics for coastal inundation mapping with the information mining abilities of the DCNN model. It can make the DCNN model suitable for the coastal inundation mapping task and will improve the mapping accuracy and robustness.

The second modification is to implement regularization to improve the model's generalization ability. For DCNN models, model overfitting limits their generalization abilities. If the model overfits, it can get very good performance on training data sets, but rather bad performance on testing data sets. Although dropout is an effective way to prevent overfitting for fully connected layers, it is often less effective for convolutional

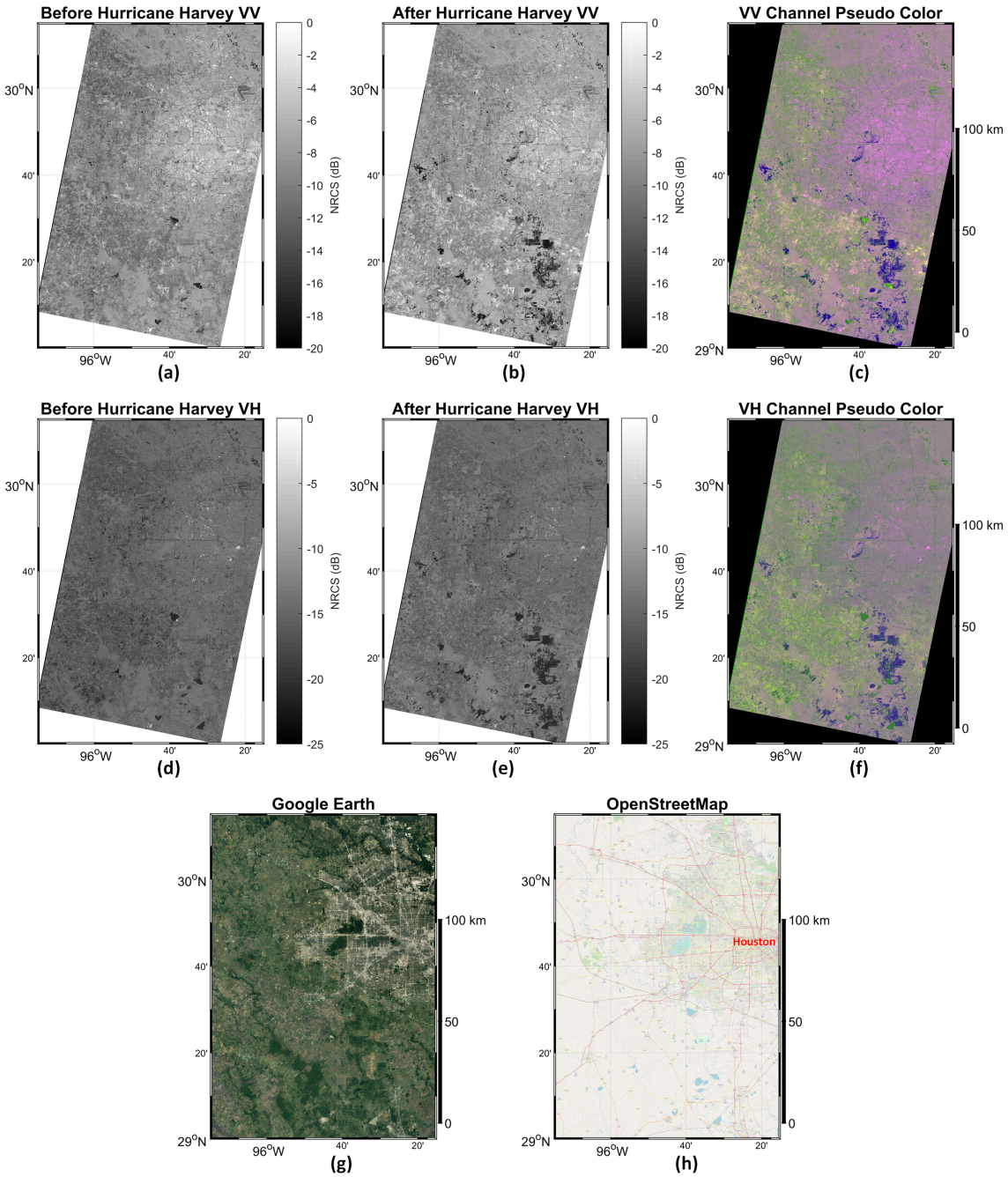


**Figure 1.** Visual illustration for the SM01 pair as an example. (a) and (b) are the preevent and postevent images for the VV polarization, respectively. (c) Pseudocolor image for the VV polarization. (d) and (e) are the preevent and postevent images for the VH polarization, respectively. (f) Pseudocolor image for the VH polarization. (g) Google Earth image in the area covered by the SM01. (h) OpenStreetMap in the area covered by the SM01.

layers (Ghiasi et al., 2018). Motivated by Tompson et al. (2014), in the proposed SARCFMNet, we add the SpatialDropout2D (SD2D) layer before the classification layer, as shown in Figure 2, to implement regularization to improve the model's robustness.

## 4. Results and Discussions

### 4.1. Validation of SARCFMNet Performance

As listed in Table 1, in all six pairs, we generate 10,049 samples. We randomly select about 20% samples from each pair to create a data set with 2,000 samples, denoted as the S2000 data set. In the training process, the

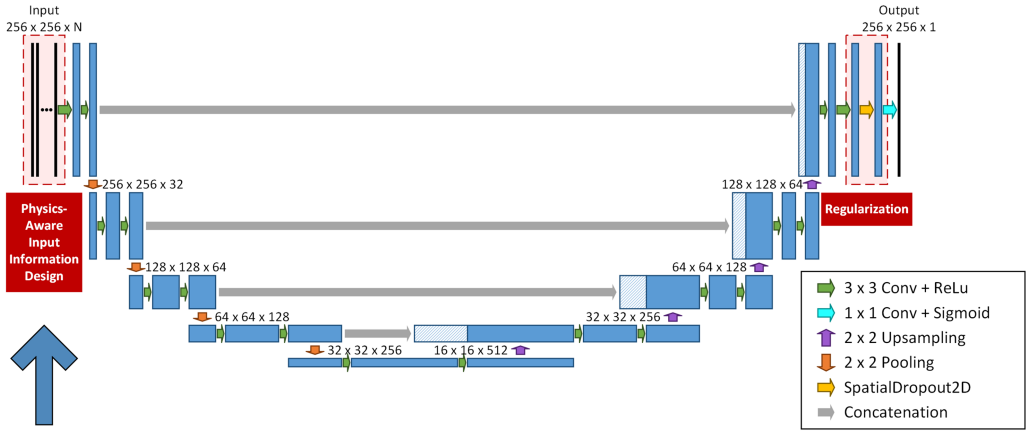


| Channels | Information | Channel number | Notation |
|---|---|---|---|
| $\sigma_{VV}^{pre}, \sigma_{VV}^{post}$ | Bi-temporal | 2 | VV |
| $\sigma_{VV}^{pre}, \sigma_{VV}^{post}, \sigma_{VV}^{post} - \sigma_{VV}^{pre}$ | Bi-temporal + Log-ratio | 3 | VV + Diff |
| $\sigma_{VH}^{pre}, \sigma_{VH}^{post}$ | Bi-temporal | 2 | VH |
| $\sigma_{VH}^{pre}, \sigma_{VH}^{post}, \sigma_{VH}^{post} - \sigma_{VH}^{pre}$ | Bi-temporal + Log-ratio | 3 | VH + Diff |
| $\sigma_{VV}^{pre}, \sigma_{VV}^{post}, \sigma_{VH}^{pre}, \sigma_{VH}^{post}$ | Bi-temporal + Dual-Polarization | 4 | DUAL |
| $\sigma_{VV}^{pre}, \sigma_{VV}^{post}, \sigma_{VV}^{post} - \sigma_{VV}^{pre}, \sigma_{VH}^{pre}, \sigma_{VH}^{post}, \sigma_{VH}^{post} - \sigma_{VH}^{pre}$ | Bi-temporal + Log-ratio + Dual-Polarization | 6 | DUAL + Diff |

**Figure 2.** Flowchart of the proposed SARCFMNet. The two specially tailored modifications to U-Net are highlighted.

S2000 data set is divided into two groups: 70% (1,400 samples) for training and 30% (600 samples) for validation. The parameter for the SpatialDropout2D is set to 0.5. Therefore, in the following performance presentation, the result with the SpatialDropout2D is denoted as _SD2D0.5. In this study, the training and testing of the network are implemented by Keras. We use Keras's default Adam optimizer. The batch size is set to 32, and the number of epochs is set to 300. The model parameters are determined by minimizing the validation loss.

The performance curves on the training and validation groups of the S2000 data set are shown in Figure 3. In this figure, each subfigure is composed of the loss and accuracy curves. This figure shows the performance comparison in the following three aspects:

1. In subfigures (a), (b), and (c), we compare the input information designs VV and VV+Diff, VH and VH +Diff, and DUAL and DUAL+Diff. In these three subfigures, we can observe, from the comparison of validation losses and validation accuracies, VV+Diff, VH+Diff, and DUAL+Diff are better than VV, VH, and DUAL, respectively. The log-ratio information can improve the mapping performance, and should be included in the input information.
2. In subfigure (d), we compare the input information designs VV+Diff, VH+Diff, and DUAL+Diff. In this subfigure, from the comparison of validation losses and validation accuracies, DUAL+Diff is better than VH+Diff, and VH+Diff is better than VV+Diff. The dual-polarization fusion can improve the mapping performance, and should be considered in practical use.
3. In subfigure (e), we compare the input information design DUAL+Diff without regularization and with SpatialDropout2D for regularization. In this subfigure, we can observe that, with regularization, the validation performance is very close to the training performance. Even though the training performance with regularization is worse than the training performance without regularization, the validation performance with regularization is better than the validation performance without regularization. This indicates that the regularization can improve the model's generalization ability in practical use and should be applied.

In Table 2, the model trained on the S2000 data set is applied on the data sets listed in Table 1. The column name indicates the input information design and if the regularization is applied. The row name indicates on which data set the trained model is applied. In each block, there are four numbers. They are classification accuracy, recall, precision, and F1 score. Recall is the ratio of the pixel number of correctly detected

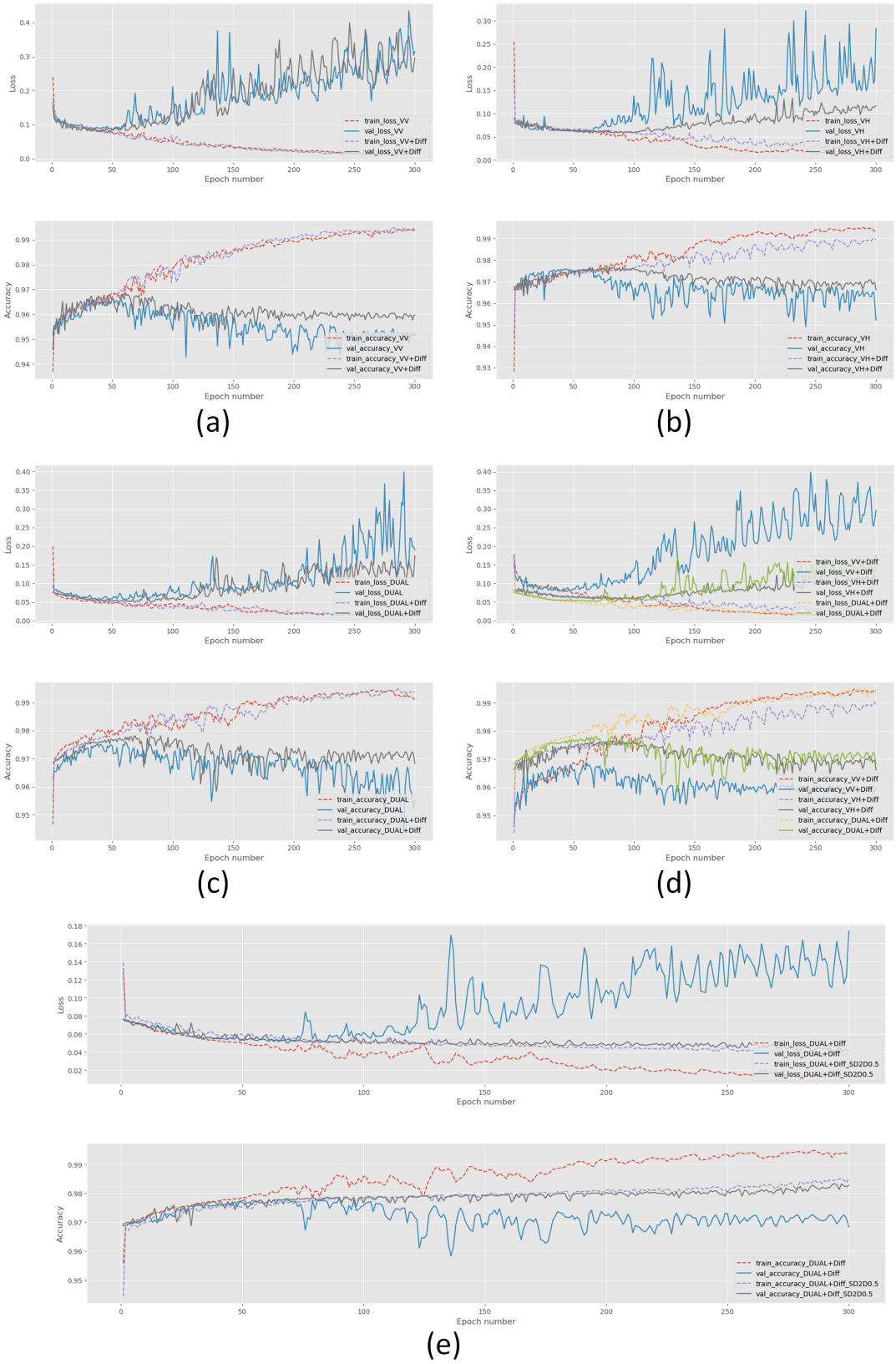


**Figure 3.** Loss and accuracy curves on the training and validation groups of the S2000 data set. (a) Comparison between VV and VV+Diff. (b) Comparison between VH and VH+Diff. (c) Comparison between DUAL and DUAL+Diff. (d) Comparison between VV+Diff, VH+Diff, and DUAL+Diff. (e) Comparison between DUAL +Diff and DUAL+Diff_SD2D0.5.

**Table 2**
*Coastal Flooding Mapping Performance Comparison on the Data Sets*

| | VV +Diff | VH +Diff | DUAL +Diff | DUAL +Diff_SD2D0.5 |
|---|---|---|---|---|
| IW01 | 0.9677 | 0.9651 | 0.9754 | **0.9810** |
| | 0.8045 | 0.7226 | 0.8388 | 0.8849 |
| | 0.8922 | 0.9489 | 0.9313 | 0.9393 |
| | 0.8461 | 0.8204 | 0.8826 | **0.9113** |
| IW02 | 0.9861 | 0.9897 | **0.9916** | 0.9907 |
| | 0.8947 | 0.7831 | 0.9087 | 0.9172 |
| | 0.7970 | 0.9647 | 0.8932 | 0.8678 |
| | 0.8430 | 0.8645 | **0.9009** | 0.8918 |
| IW03 | 0.9350 | 0.9685 | 0.9684 | **0.9741** |
| | 0.6395 | 0.8996 | 0.9184 | 0.9541 |
| | 0.6507 | 0.7889 | 0.7793 | 0.8025 |
| | 0.6451 | 0.8406 | 0.8432 | **0.8718** |
| IW04 | 0.9817 | **0.9932** | 0.9904 | 0.9912 |
| | 0.9143 | 0.8529 | 0.9301 | 0.8721 |
| | 0.6593 | 0.9324 | 0.8066 | 0.8598 |
| | 0.7661 | **0.8909** | 0.8640 | 0.8659 |
| IW05 | 0.9647 | 0.9719 | 0.9728 | **0.9824** |
| | 0.8888 | 0.9151 | 0.9641 | 0.9397 |
| | 0.6193 | 0.6763 | 0.6718 | 0.7790 |
| | 0.7300 | 0.7778 | 0.7918 | **0.8518** |
| SM01 | 0.9866 | 0.9823 | 0.9912 | **0.9915** |
| | 0.8580 | 0.6750 | 0.8816 | 0.8909 |
| | 0.8867 | 0.9907 | 0.9492 | 0.9467 |
| | 0.8721 | 0.8029 | 0.9142 | **0.9180** |
| Weighted Average | 0.9681 | 0.9771 | 0.9800 | **0.9842** |
| | 0.8306 | 0.8219 | 0.9098 | 0.9118 |
| | 0.7363 | 0.8649 | 0.8230 | 0.8575 |
| | 0.7737 | 0.8313 | 0.8583 | **0.8815** |

[a]The bold emphasis signifies the best performance in each row.

flooding areas to the pixel number of ground truth. Precision is the ratio of the pixel number of correctly detected flooding areas to the pixel number of predicted flooding areas. A higher recall value means the model misses less flooding areas. A higher precision value means the model extracts less false alarms. F1 score is the harmonic mean of recall and precision. The last row is the weighted average of the performances on the above six data sets. The weights are the sample number proportions in the total sample number of the six data sets. In each row, the best classification accuracy and F1 score are highlighted in bold. From this table, we can have two observations: (1) the dual-polarization fusion improves the mapping performance and (2) the regularization improves the model's generalization ability. These are consistent with the above observations from Figure 3.

Figure 4 gives the visual presentation of the flooding mapping performance on the SM01 data set, which we select as an example for presentation. Subfigures (a) and (b) show the ground truth and predicted flooding mapping with the SARCFMNet (DUAL+Diff_SD2D0.5). By comparing (a) and (b), the predicted mapping is very close to the ground truth, which visually confirms the effectiveness of the proposed method.

### 4.2. Geospatial and Temporal Analysis of Flooding

Based on the flooding mapping products generated by the SARCFMNet, the geospatial and temporal analyses of the coastal flooding caused by Harvey are performed.

We select the flooding mapping product of the SM01 pair, as shown in Figure 4b, to perform the geospatial analysis. The ancillary data for the geospatial analysis are the U.S. Geological Survey (USGS) National Elevation Dataset (USGS National Map, n.d.), the 2016 National Land Cover Database (Yang et al., 2018), and the water occurrence of the Global Surface Water Mapping Dataset (Pekel et al., 2016). They are shown in Figures 4d–4f. The National Land Cover Database legend is shown in Figure 4g.

Based on the flooding mapping product and ancillary data, we can get the following geospatial analysis conclusions:

1. The flooding area is about 284 $km^2$ and accounts for about 3% of the whole scene. After filtering the flooding mapping product with a simple filter (disk shape, radius = 100 pixels), we can generate a flooding heat map, which is superimposed onto the preevent SAR imagery and shown in Figure 4c. The heat map clearly shows the severity of the flooding. The most severely flooded areas are in the southern part of Houston.
2. The flooded area elevation and the scene elevation distributions are shown in Figure 4h, generated from Figure 4d. It shows the flooded area elevation is distinctly lower than the scene elevation. The flooding is more likely to happen and stay in places with lower elevation.
3. The proportions of land cover types in the flooded areas are shown in Figure 4i, generated from Figure 4e. It shows the dominant land cover types in the flooded areas are pasture and cultivated crops. Their combined proportion is higher than 76%. It means that the flooding had a huge negative impact on agriculture.
4. The history water occurrence distribution in the flooded areas is shown in Figure 4j, generated from Figure 4f. It shows the history water occurrence in the flooded areas is very close to 0. It means the extracted areas represent an extremely abnormal situation, and people should be alert to this situation.

The flooding mapping products from IW01, IW04, IW05, and SM01 have an overlapped area. We use this overlapped area to perform the temporal analysis of the flooding. The temporal analysis result is shown in Figure 5. The product sequence is described by the calendar in the lower right of this figure. The upper part of this figure shows the flooding duration probability of the overlapped area. It can help us to see the

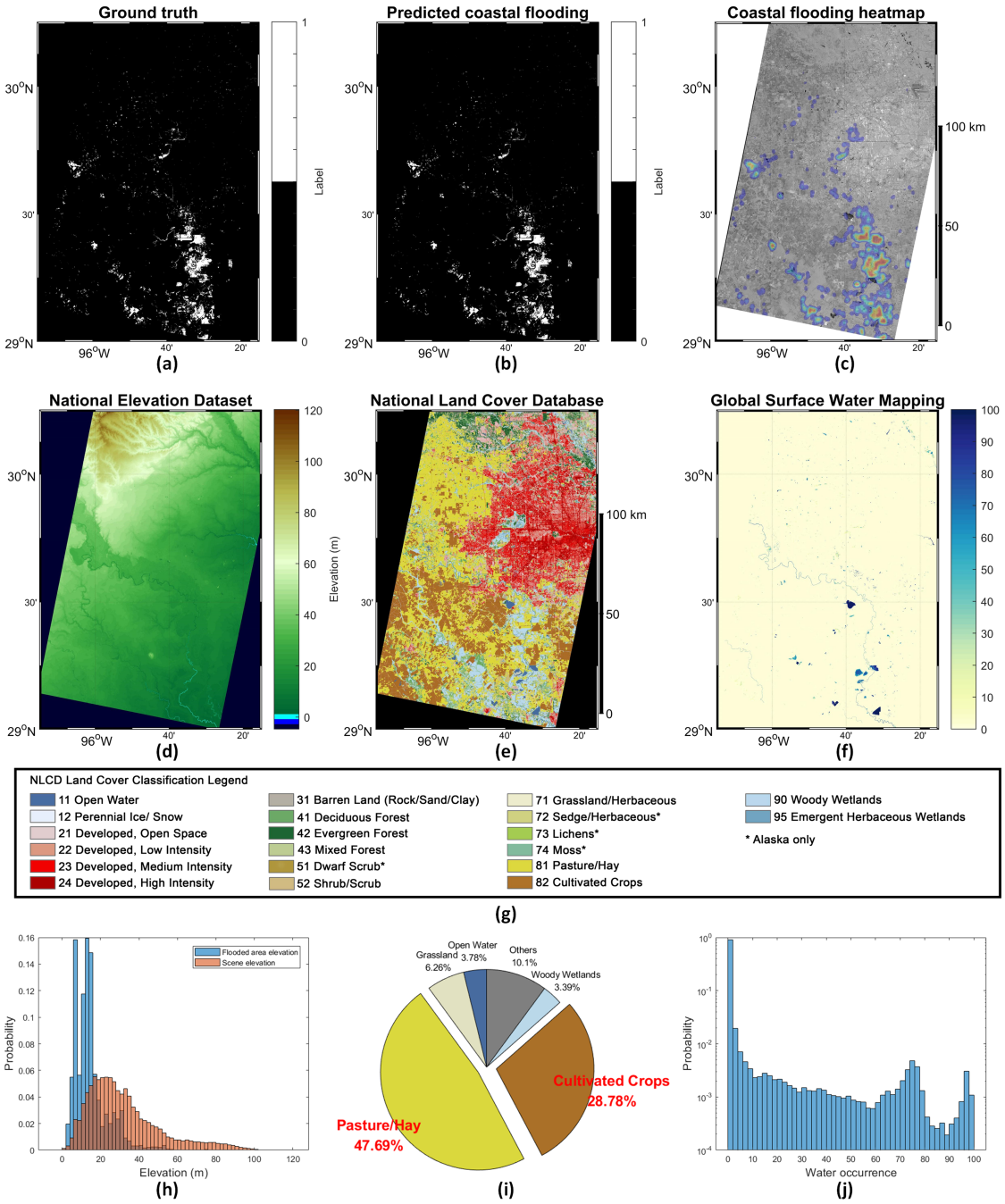


**Figure 4.** Geospatial analysis of the flooding product of the SM01 data set. (a) Ground truth. (b) Flooding mapping product with the SARCFMNet. (c) Generated flooding heat map superimposed onto the preevent SAR imagery. (d) Elevation from the National Elevation Dataset. (e) Land cover from the 2016 National Land Cover Database. (f) Water occurrence from the Global Surface Water Mapping Dataset. (g) Legend of (e). (h) Flooded area elevation and scene elevation distributions. (i) Land cover type proportions in the flooded areas. (j) Water occurrence distribution in the flooded areas.

temporal evolvement of flooding in this area. The flooded areas with the highest probability are the last disappeared flooded areas. The areas with probability lower than zero are the areas without data in one product.

Normally, the flooded areas shrink over time in the product sequence as described by the flooded area proportions in the lower middle part of Figure 5. The shrinking rate is about 1% of the analyzed area per day (about 23 $km^2$ per day). By analyzing the product sequence, however, we discovered a phenomenon of

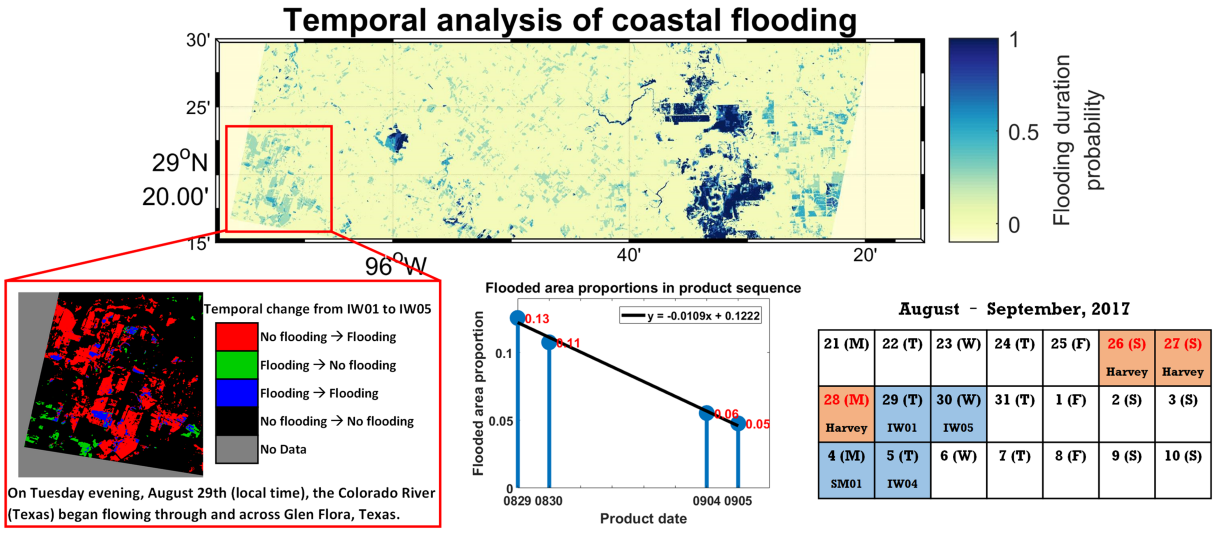


**Figure 5.** Temporal analysis of the flooding mapping products. Upper: flooding duration probability map. Lower left: temporal change of flooding products from IW01 to IW05 is consistent with the flooding fact in Glen Flora, Texas. Lower middle: flooded area proportions in the flooding product sequence normally show the flooding shrinking. Lower right: flooding product sequence calendar.

delayed flooding. There is one flooded area, which is not shown in the product of IW01 but shown in the product of IW05. This area is highlighted by the red rectangle. The temporal change of flooding from IW01 to IW05 is shown in the lower left part of Figure 5. This area represents Glen Flora, Texas. We search for the local news (Glen Flora Emporium, n.d.) and find that, in the evening of August 29 (local time), the Colorado River (Texas) overflowed its banks and began flowing through and across Glen Flora. This is why the flooded area is not captured by IW01 (00:26 UTC, 29 August) but captured by IW05 (12:22 UTC, 30 August).

### 4.3. Wind Influence Analysis

In this part, we discuss a problem which is seldom considered in flooding mapping studies: the wind influence. This is a practical problem in hurricane-induced coastal flooding mapping. For coastal flooding mapping, we may face a situation: The hurricane has already caused heavy rain and flooding in the coastal area, but it has not left the area and still brings strong wind. In this situation, the strong wind might interfere with the flooding mapping in this scene, because the strong wind could increase the water areas' NRCS. As discussed above, the postevent image of the IW01 pair is influenced by wind. Here, we use an experiment to discuss the wind influence in the DCNN-based coastal flooding mapping.

From the data sets IW01 and IW03, we randomly select 400 samples from each to generate two data sets, IW01_selected and IW03_selected, respectively. We train two models on IW01_selected and IW03_selected with the DUAL+Diff design. Then, we test the two models on the data sets IW01 and IW03. The results are listed in Table 3. In this table, the column name indicates on which data set the model is trained, and the row name indicates on which data set the model is tested. In each block, there are three numbers. They are classification accuracy, recall, and precision. On the diagonal of the table, the results represent the situation of training and testing on the same scene. The performances are good. But the performances outside the diagonal drop drastically. The model trained on IW01_selected and tested on IW03 shows low precision. This is because the model is trained on the IW01_selected, and the postevent image of the IW01_selected is influenced by a strong wind. In this case, the trained model tends to "think" the water areas in the postevent image should have higher NRCS values, which causes many false alarms in the IW03 and lower precision. Similarly, we can explain why the model trained on the IW03_selected and tested on the IW01 has low recall.

**Table 3**
*Wind Influence Analysis Results*

| | IW01_selected | IW03_selected |
|---|---|---|
| IW01 | 0.9875 | 0.9599 |
| | 0.9405 | *0.6722* |
| | 0.9459 | 0.9502 |
| IW03 | 0.9596 | 0.9887 |
| | 0.9252 | 0.9441 |
| | *0.7186* | 0.9347 |

[a]Italic emphasis signifies some performance results.

**Table 4**
*Cost-Sensitive Loss Analysis Results*

| | Trained on IW01_selected, Tested on IW01 | Trained on IW03_selected, Tested on IW03 |
|---|---|---|
| BCE | 0.9875 | 0.9887 |
| | 0.9405 | 0.9441 |
| | 0.9459 | 0.9347 |
| $\alpha$BBCE ($\alpha = 0.8$) | 0.9785 | 0.9846 |
| | *0.9858* | *0.9848* |
| | 0.8453 | 0.8670 |
| F$\beta$ ($\beta = 2$) | 0.9741 | 0.9540 |
| | *0.9724* | *0.9808* |
| | 0.8242 | 0.6720 |
| F$\beta$ ($\beta = 0.5$) | 0.9835 | 0.9798 |
| | 0.8838 | 0.8374 |
| | *0.9635* | *0.9372* |

[a]Italic emphasis signifies some performance results.

This experiment demonstrates the wind influence in the DCNN-based coastal flooding mapping. As listed in Table 2, since the S2000 data set is generated from different wind conditions, the trained model has more balanced performances. We could still see the wind influence from the results, especially from the results on the IW01 and IW03. This indicates that the DCNN models considering different wind conditions will be more robust and practical.

### 4.4. Cost-Sensitive Loss Analysis

In this part, we still use the two data sets IW01_selected and IW03_selected from the last part to discuss the cost-sensitive losses for the DCNN-based coastal flooding mapping. First, we use the default BCE loss with the DUAL+Diff design and the results are listed in Table 4. In each block, there are three numbers. They are classification accuracy, recall, and precision. We can observe, in the coastal flooding mapping, the BCE loss can balance precision and recall.

In practical use, a cost-sensitive loss is usually needed. If the cost of low recall is very high, that is, the cost of missed detections is very high, the trained model needs to improve its recall as much as possible. Similarly, if the cost of low precision is very high, that is, the cost of false alarms is very high, the trained model needs to improve its precision as much as possible. In the DCNN models, the cost-sensitive losses can satisfy these needs. One way of designing the cost-sensitive loss is the $\alpha$-balanced BCE ($\alpha$BBCE) loss (Lin et al., 2017):

$$L_{\alpha\text{BBCE}} = -\frac{1}{N}\sum_{i=1}^{N}\{\alpha y_i \log\widehat{y}_i + (1-\alpha)(1-y_i)\log(1-\widehat{y}_i)\} \tag{1}$$

where $y_i$ denotes the ground-truth label of the $i$th pixel, 1 for flooding and 0 for background, $\widehat{y}_i$ denotes the predicted probability of the $i$th pixel being flooding, and $N$ is the pixel number. $\alpha \in [0,1]$ is the weight. As $\alpha$ is higher, the model's accuracy in flooded areas is given a greater weight during training. A higher value for $\alpha$ is reasonable, considering that the pixel number of flooding is much smaller than that of the background. In this experiment, $\alpha$ is set to 0.8. As listed in Table 4, the $\alpha$BBCE loss is effective. The recall is improved at the expense of precision.

Another way of designing the cost-sensitive loss is the F$\beta$ loss:

$$L_{\text{F}\beta} = 1-\underbrace{\left(1+\beta^2\right)\frac{P\cdot R}{\beta^2\cdot P + R}}_{\text{F}\beta\text{ score}} \tag{2}$$

where $P$ denotes precision and $R$ denotes recall. Minimizing the F$\beta$ loss equals maximizing the F$\beta$ score, where $\beta$ is a positive real weight. If $\beta > 1$, optimizing recall is given a greater weight during training. If $\beta < 1$, optimizing precision is given a greater weight. The results of the F$\beta$ loss, $\beta = 2$ and $\beta = 0.5$, are listed in Table 4. The results demonstrate the F$\beta$ loss is effective for adaptive performance adjustment according to performance costs. For $\beta = 2$, recall is improved at the expense of precision. For $\beta = 0.5$, precision is improved at the expense of recall.

In this part, we discuss the cost-sensitive loss designs for the DCNN-based coastal flooding mapping. These designs are adaptive according to performance costs. It is worth noting that there are two expenses: (1) there is performance trade-off and (2) there is one more hyperparameter should be predefined.

## 5. Conclusions

In this paper, we present the SARCFMNet model to mine bitemporal and dual-polarization SAR image information for coastal flooding mapping. The SARCFMNet is based on the U-Net framework, but we specially tailor it for the SAR coastal flooding mapping problem, with two modifications: the physics-aware input

information design and the regularization. The proposed SARCFMNet is applied to the mapping and impact analysis of the coastal inundation caused by Hurricane Harvey near the Houston area. After processing a total area of 140,000 $km^2$ from six pairs of Sentinel-1 SAR images, the SARCFMNet model achieves an accuracy rate of 0.98 and an F1 score of 0.88. It shows better and more robust performance, compared to the classic and widely applied U-Net model. The SARCFMNet model is more suitable for the SAR coastal inundation mapping task. Based on the mapping products, the geospatial analysis of Harvey-caused inundation is performed and shows its huge impact on agriculture. The multitemporal analysis calculates the inundation shrinking rate and discovers a phenomenon of delayed inundation in Glen Flora, Texas. In addition, the wind influence is revealed in the DCNN-based method, which indicates the DCNN models considering wind influence will be more practical. The cost-sensitive losses for the DCNN-based coastal flooding mapping are explored, which is useful for more adaptive designs according to performance costs. In the SARCFMNet model, the features for robust classification are mined from data automatically, instead of being predesigned and predefined. This indicates, in other multitemporal SAR imagery classification applications, the proposed model can also be utilized. The users only need to modify the training samples according to their actual problems.

## Data Availability Statement

The Sentinel-1 data used in this study are available from the Copernicus Open Access Hub. Registered users can download these data from the Hub's online service (https://scihub.copernicus.eu/) for free. The USGS National Elevation Dataset, the National Land Cover Database, and the Global Surface Water Mapping Dataset used in this study are available from the GEE. Registered users can download these data from the GEE's online service (https://code.earthengine.google.com/) for free. The Copernicus EMS Rapid Mapping products used in this study are available from the Copernicus EMS. Users can download these data from the EMS's online service (https://emergency.copernicus.eu/mapping/list-of-components/EMSR229) for free.

**Acknowledgments**
This work was supported by the Strategic Priority Research Program of the Chinese Academy of Sciences (XDA19090103), the Chinese Postdoctoral Science Foundation (2019M651474), the National Natural Science Foundation of China (41676167), the Project of State Key Laboratory of Satellite Ocean Environment Dynamics, Second Institute of Oceanography (SOEDZZ1804), and the National Key R&D Program of China (2016YFC1401007). The authors would like to thank the European Space Agency for providing the Sentinel-1 data and the Sentinel Application Platform software, thank the Google Earth Engine (GEE) for providing the USGS National Elevation Dataset, the National Land Cover Database, and the Global Surface Water Mapping Dataset, and thank the Copernicus EMS for providing the Rapid Mapping products.

## References

Anantrasirichai, N., Biggs, J., Albino, F., Hill, P., & Bull, D. (2018). Application of machine learning to classification of volcanic deformation in routinely generated InSAR data. *Journal of Geophysical Research: Solid Earth*, *123*, 6592–6606. https://doi.org/10.1029/2018JB015911

Bazi, Y., Bruzzone, L., & Melgani, F. (2005). An unsupervised approach based on the generalized Gaussian model to automatic change detection in multitemporal SAR images. *IEEE Transactions on Geoscience and Remote Sensing*, *43*(4), 874–887.

Bilskie, M. V., Hagen, S. C., Medeiros, S. C., & Passeri, D. L. (2014). Dynamics of sea level rise and coastal flooding on a changing landscape. *Geophysical Research Letters*, *41*, 927–934. https://doi.org/10.1002/2013GL058759

Chini, M., Hostache, R., Giustarini, L., & Matgen, P. (2017). A hierarchical split-based approach for parametric thresholding of SAR images: Flood inundation as a test case. *IEEE Transactions on Geoscience and Remote Sensing*, *55*(12), 6975–6988.

Copernicus EMS Rapid Mapping. (n.d.). https://emergency.copernicus.eu/mapping/list-of-components/EMSR229. (Accessed: 2019-08-09)

Ghiasi, G., Lin, T.-Y., & Le, Q. V. (2018). DropBlock: A regularization method for convolutional networks. arXiv:1810.12890 [cs].

Giustarini, L., Hostache, R., Kavetski, D., Chini, M., Corato, G., Schlaffer, S., & Matgen, P. (2016). Probabilistic flood mapping using synthetic aperture radar data. *IEEE Transactions on Geoscience and Remote Sensing*, *54*(12), 6958–6969.

Glen Flora Emporium. (n.d.). https://heartofatexan.com/stories/hurricane-harvey-glen-flora-emporium. (Accessed: 2019-07-22)

Horritt, M. (1999). A statistical active contour model for SAR image segmentation. *Image and Vision Computing*, *17*(3-4), 213–224.

Hostache, R., Chini, M., Giustarini, L., Neal, J., Kavetski, D., Wood, M., et al. (2018). Near-real-time assimilation of SAR-derived flood maps for improving flood forecasts. *Water Resources Research*, *54*, 5516–5535. https://doi.org/10.1029/2017WR022205

Kang, W., Xiang, Y., Wang, F., Wan, L., & You, H. (2018). Flood Detection in Gaofen-3 SAR images via fully convolutional networks. *Sensors*, *18*(9), 2915.

Lin, T., Goyal, P., Girshick, R., He, K., & Dollr, P. (2017). Focal Loss for Dense Object Detection. In 2017 IEEE International Conference on Computer Vision (ICCV) (pp. 2999--3007).

Matgen, P., Hostache, R., Schumann, G., Pfister, L., Hoffmann, L., & Savenije, H. H. G. (2011). Towards an automated SAR-based flood monitoring system: Lessons learned from two case studies. *Physics and Chemistry of the Earth, Parts A/B/C*, *36*(7-8), 241–252.

Park, S.-E., Yamaguchi, Y., & Kim, D.-j. (2013). Polarimetric SAR remote sensing of the 2011 Tohoku earthquake using ALOS/PALSAR. *Remote sensing of Environment*, *132*, 212–220.

Patricola, C. M., & Wehner, M. F. (2018). Anthropogenic influences on major tropical cyclone events. *Nature*, *563*(7731), 339–346. https://doi.org/10.1038/s41586-018-0673-2

Pekel, J.-F., Cottam, A., Gorelick, N., & Belward, A. S. (2016). High-resolution mapping of global surface water and its long-term changes. *Nature*, *540*(7633), 418–422. https://doi.org/10.1038/nature20584

Plank, S., Jüssi, M., Martinis, S., & Twele, A. (2017). Mapping of flooded vegetation by means of polarimetric Sentinel-1 and ALOS-2/PALSAR-2 imagery. *International Journal of Remote Sensing*, *38*(13), 3831–3850.

Reichstein, M., Camps-Valls, G., Stevens, B., Jung, M., Denzler, J., Carvalhais, N., & Prabhat (2019, February). Deep learning and process understanding for data-driven Earth system science. *Nature*, *566*(7743), 195–204. https://doi.org/10.1038/s41586-019-0912-1

Ronneberger, O., Fischer, P., & Brox, T. (2015). U-net: Convolutional networks for biomedical image segmentation. In *International Conference on Medical image computing and computer-assisted intervention* (pp. 234–241). Basel, Switzerland: Springer.

Rudner, T. G. J., Ruwurm, M., Fil, J., Pelich, R., Bischke, B., Kopackova, V., & Bilinski, P. (2018). Multi3Net: Segmenting flooded buildings via fusion of multiresolution, multisensor, and multitemporal satellite imagery. arXiv:1812.01756 [cs]. Retrieved from http://arxiv.org/abs/1812.01756

Russakovsky, O., Deng, J., Su, H., Krause, J., Satheesh, S., Ma, S., et al. (2015). Imagenet large scale visual recognition challenge. *International Journal of Computer Vision*, *115*(3), 211–252. https://doi.org/10.1007/s11263-015-0816-y

Sato, M., Chen, S.-W., & Satake, M. (2012). Polarimetric SAR analysis of tsunami damage following the March 11, 2011 East Japan earthquake. *Proceedings of the IEEE*, *100*(10), 2861–2875.

Tompson, J., Goroshin, R., Jain, A., LeCun, Y., & Bregler, C. (2014, November). Efficient object localization using convolutional networks. arXiv:1411.4280 [cs].

USGS National Map. (n.d.). https://www.usgs.gov/core-science-systems/national-geospatial-program/national-map. (Accessed: 2019-08-09)

Vahedifard, F., AghaKouchak, A., & Jafari, N. H. (2016). Compound hazards yield Louisiana flood. *Science*, *353*(6306), 1374–1374. https://doi.org/10.1126/science.aai8579

van Oldenborgh, G. J., van der Wiel, K., Sebastian, A., Singh, R., Arrighi, J., Otto, F., et al. (2017). Attribution of extreme rainfall from Hurricane Harvey, August 2017. *Environmental Research Letters*, *12*(12), 124009. https://doi.org/10.1088/1748-9326/aa9ef2

Weather Underground. (n.d.). https://www.wunderground.com/hurricane/atlantic/2017/tropical-storm-harvey. (Accessed: 2019-06-25)

Yang, L., Jin, S., Danielson, P., Homer, C., Gass, L., Bender, S. M., et al. (2018). A new generation of the United States national land cover database: Requirements, research priorities, design, and implementation strategies. *ISPRS Journal of Photogrammetry and Remote Sensing*, *146*, 108–123. https://doi.org/10.1016/j.isprsjprs.2018.09.006

Zhang, J., Liu, P., Zhang, F., & Song, Q. (2018). CloudNet: Ground-based cloud classification with deep convolutional neural network. *Geophysical Research Letters*, *45*, 8665–8672. https://doi.org/10.1029/2018GL077787

Zhang, W., Villarini, G., Vecchi, G. A., & Smith, J. A. (2018, November). Urbanization exacerbated the rainfall and flooding caused by Hurricane Harvey in Houston. *Nature*, *563*(7731), 384–388. https://doi.org/10.1038/s41586-018-0676-z